ADVANCED ENERGY MATERIALS
www.advenergymat.de

Conjugated Imine Polymer Synthesized via Step-Growth Metathesis for Highly Stable Silicon Nanoparticle Anodes in Lithium-Ion Batteries

Trevor R. Martin, Leah Rynearson, Mackenzie Kuller, Joseph Quinn, Chongmin Wang, Brett Lucht, and Nathan R. Neale*

This work reports a new method to synthesize polyphenylmethanimine (polyPMI) as a linear or a hyperbranched, conjugated polymer using an aldehyde-imine metathesis reaction. This work details the reaction mechanisms of this polymerization by characterizing a red-shift in its absorption spectrum as polymer conjugation length increases and verifies that this optical shift results from extended π-condensation using density functional theory. This new synthetic approach provides a polymer that can potentially be depolymerized for facile recyclability and is compatible with air- and water-sensitive chemistries. As an example of the utility of this new approach, this work demonstrates that this polymer can be directly grown on silicon nanoparticles to create silicon anodes for lithium-ion batteries with a high degree of electrochemical interfacial passivation. These silicon anodes exhibit Coulombic efficiencies above 99.9% and can accommodate silicon nanoparticle expansion and contraction during lithiation and delithiation as demonstrated by stable reversible capacities for 500 cycles. Finally, this work demonstrates that polyPMI facilitates the formation of a lithium fluoride rich solid electrolyte interphase that remains chemically and mechanically stable after long term cycling.

1. Introduction

Conjugated polymers (CPs) have driven innovations in a variety of energy conversion and storage fields including organic photovoltaics (OPVs),[1,2] supercapacitors,[3] transistors,[2] thermoelectrics,[2] lithium ion batteries (LIBs),[3,4] and other metal cation battery systems.[3,4] Recently, CP research has increasingly focused on developing novel, simplified reaction schemes as an alternative to costly multi-step synthetic procedures with traditionally catalyzed cross-coupling reactions that may be difficult to implement at scale.[5] For example, previous reports have demonstrated that OPV cost scales directly with the number of synthetic steps,[6] and significant effort has been dedicated toward developing new, comparatively simple polymerization methods such as direct heteroarylation to produce conjugated polymers.[5,7]

Within the LIB field, polyaniline is frequently utilized as a CP active material for electrodes to produce organic batteries.[3,4] Similarly, imine-based covalent organic frameworks (COFs) have received significant interest as a new class of materials for energy storage applications, including as promising LIB electrode materials.[8] These materials are typically synthesized using a combination of condensation reactions,[8–12] acid-catalyzed conditions,[8,10–12] autoclave-based methods,[13,14] or microwave-assisted synthetic procedures,[11] which are often not compatible with other fragile nanoscale materials that may be susceptible to oxidation or degradation in harsh synthetic conditions. Imine-based CPs have been previously synthesized using condensation reactions and are an important foundational material within the field,[15] however these reactions are not compatible with other water or oxygen sensitive materials and have therefore remained inaccessible for a variety of applications. The novel imine metathesis reaction that we have developed is a universal approach that is compatible with materials that are unstable to these conditions.

Various polymers have been developed to improve the performance of silicon anodes by modifying polyacrylic acid,[16–19] by forming various cross-linked polymers,[20–23] by forming cyclized polyacrylonitrile groups,[24] by polycondensation,[25] by adding commercially available polythiophenes,[26] or by using traditionally cross-coupled polymerizations.[27] Drawing inspiration from direct heteroarylation and imine-based COF synthetic methods, we have developed a novel method to synthesize hyperbranched, conjugated imine polymers compatible

T. R. Martin, M. Kuller, N. R. Neale
Chemistry and Nanoscience Center
National Renewable Energy Laboratory
Golden, CO 80401, USA
E-mail: tmartin@nrel.gov
L. Rynearson, B. Lucht
Department of Chemistry
University of Rhode Island
Kingston, RI 02881, USA
J. Quinn, C. Wang
Environmental Molecular Sciences Laboratory
Pacific Northwest National Laboratory
Richland, WA 99354, USA
The ORCID identification number(s) for the author(s) of this article can be found under https://doi.org/10.1002/aenm.202203921.

DOI: 10.1002/aenm.202203921

with water- and air-sensitive materials. This method is based on stepwise reactions to form an alkylimine precursor that is subjected to a metathesis reaction with an aldehyde resulting in an alkyl aldehyde rather than a water byproduct. This aldehyde-imine metathesis reaction affords a simple route to both linear and branched conjugated oligomeric coatings that have the potential to be useful for a variety of applications given the imine group's inherent recyclable/depolymerizable nature as well as compatibility with water- and oxygen-sensitive species. To demonstrate the utility of this novel synthetic approach, we leverage this aldehyde-imine metathesis reaction for making CPs in LIBs using silicon nanoparticles as the active anode material. More broadly, our results demonstrate a new class of simple step-growth CPs with potential utility for a variety of energy conversion, storage, or recycling[28] applications previously inaccessible for imine-based CPs.

2. Results and Discussion

Scheme 1a illustrates a conventional approach wherein benzene-1,4-dicarboxaldehyde (terephthalaldehyde, TPA) undergoes a condensation reaction with phenylenediamine (PDA) to produce polyphenylmethanimine (polyPMI) and water as the reaction byproduct. Our newly developed method is a two-step synthetic route to a similar polyPMI CP. In this new methodology, an alkylimine precursor is first synthesized by reacting PDA with hexanal (hexaldehyde) via a simple condensation reaction as shown in Scheme 1b. Diglyme is chosen as a suitable solvent because of its relatively high boiling point (162 °C), its ability to dissolve polar species, and its absence of potentially reactive carbonyl moieties. Hexanal is chosen as a suitable reagent because it is the shortest alkyl aldehyde with a boiling point that is significantly above that of water (130 °C), which facilitates dehydration of the resulting hexylimine precursor. This precursor is used to effect metathesis reactions with the phenylaldehyde moieties in TPA as shown in Scheme 1c to form a polyPMI oligomer.

Figure 1a shows images of the reaction evolution of the conventional one-step process (Scheme 1a), where a systematic change in color is observed with increasing reaction time at 120 °C. The reaction progresses rapidly to produce an orange-colored polymer suspension after only 10 min, with minimal changes to the solution after this time. Figure 1b shows images of our newly developed two-step imine metathesis reaction evolution shown in Scheme 1c. Compared with the conventional condensation reaction, the two-step imine metathesis reaction progresses more slowly and continues to progress over the course of 60 min at 120 °C to produce a dark red colored polymer solution. Figure 1c shows a series of absorption spectra across the ultraviolet to visible range (UV–vis) collected over 60 min for this imine metathesis polymerization reaction (note: spectra collected at ambient temperature). The spectra show a systematic red-shift in the polymer absorption edge, indicating an increase in π-conjugation length as the reaction progresses.

To corroborate that the observed color changes are due to formation of simple π-conjugated polymers with increasing chain length, we conduct density functional theory (DFT) calculations for the polyPMI oligomers. Figure 1c shows the predicted natural transition orbitals (NTOs) for a polyPMI dimer, wherein electron orbital delocalization can be seen across the imine π-bond bridge. Figure 1d shows the predicted absorption spectra for four oligomer lengths, where the simulations predict a systematic red-shift in the absorption spectra and increase in π-conjugation length. These DFT simulations verify that the aldehyde-imine metathesis reaction is a viable route to highly conjugated polymers, apparently with greater π-conjugation length and solubility than similar polyimine polymers from the conventional imine condensation process, as evidenced by the darker color of the polymer solution show in Figure 1b.

We next probe the polymer formation mechanism using a series of proton nuclear magnetic resonance spectroscopy (^{1}H NMR) experiments. **Figure 2** shows the ^{1}H NMR spectra for the imine precursor formation using PDA and hexanal (as depicted in Scheme 1b). In addition, the relative aromatic peak positions are consistent with the formation of the proposed imine precursor structure and are similar to other reported imine polymer structures.[15,29,30] Moreover, the *j* proton peak shown in Figure 2c is consistent with the expected imine bond formation, is corroborated by the absence of a secondary amine peak at ≈4.3 ppm, and is similar to other reported imine polymer structures.[15,29,30] We attribute the unidentified peak that appears at ≈6 ppm to trace vinylic contaminants in

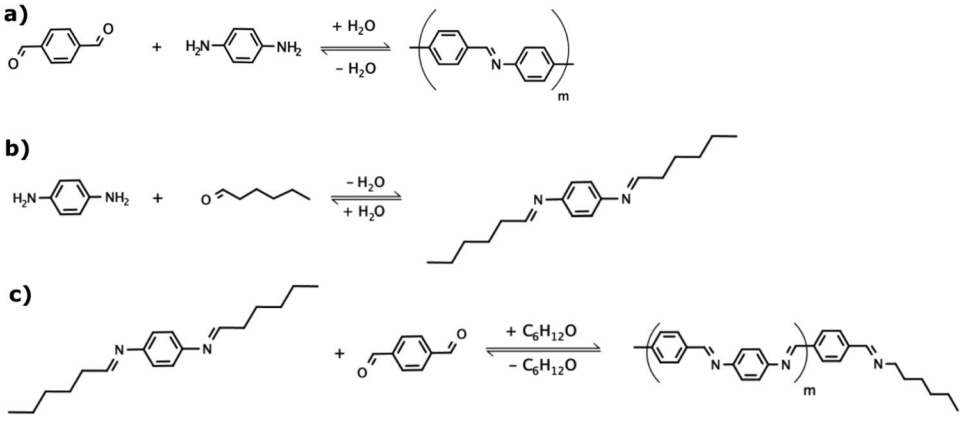

Scheme 1. a) Conventional condensation reaction of TPA and PDA precursors and our new two-step approach based on b) Condensation of PDA and hexanal to form imine precursor followed by subsequent c) Carbonyl-induced imine metathesis to form polyPMI.

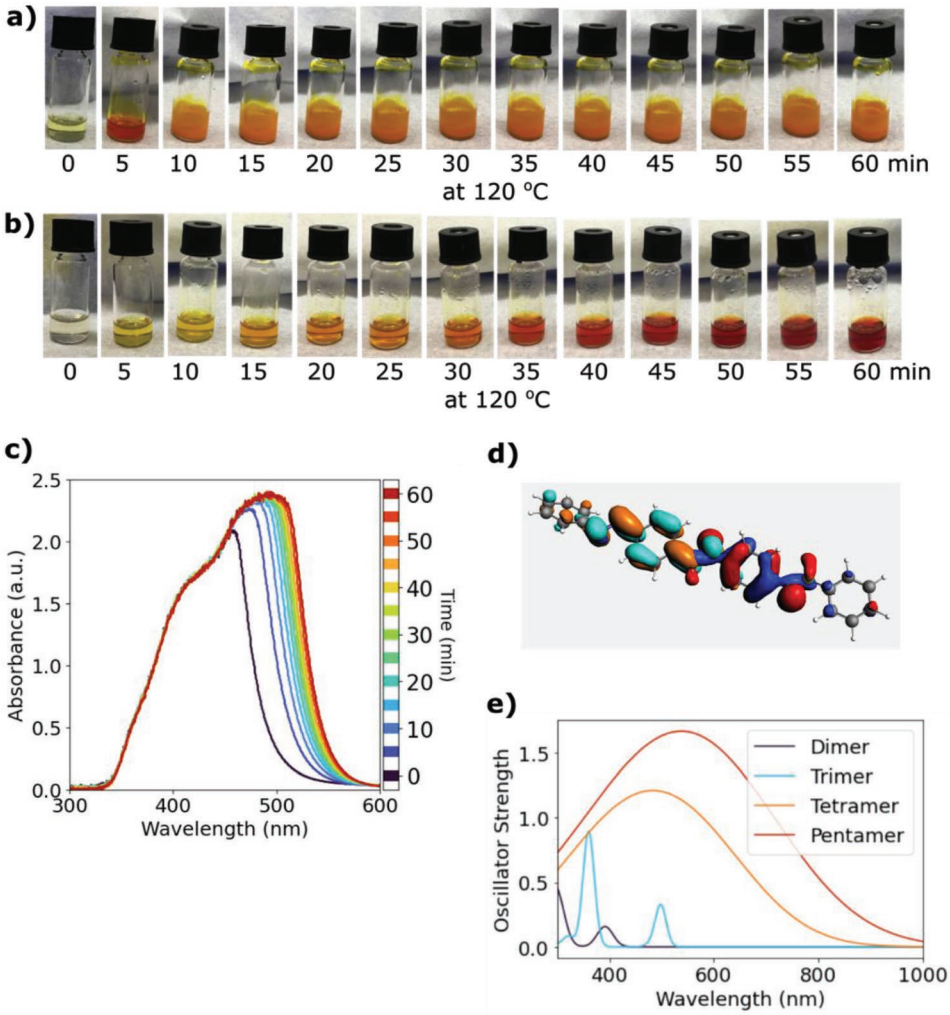

Figure 1. a) Optical images of the conventional imine condensation reaction between PDA and TPA in diglyme at 120 °C (Scheme 1a) at 5 min intervals. b) Optical images of our new imine metathesis reaction between imine precursor and TPA in diglyme at 120 °C (Scheme 1c) at 5 min intervals. c) UV–vis absorption spectra of the polyPMI formation as a function of time at ambient temperature for 60 min. d) DFT simulated NTOs resulting from electronic transitions between the HOMO ground state (blue and red colored orbitals) and the LUMO excited state (orange and cyan colored orbitals) of the tetramer. e) Predicted absorbance for four different oligomer lengths from analogous simulated excitations.

the diglyme solvent and we also note the presence of water in Figure 2a prior to dehydration.

We also extend this approach from linear to branched polymers. **Figure 3** shows the ^{1}H-NMR spectra for the polyPMI formation reaction depicted in Scheme 1c, where benzene-1,3,5-trialdehyde (BTA) is substituted for one fourth (1:3 by stoichiometric ratio of BTA:TPA) of the TPA in the imine metathesis reaction. For Figure 3c, the broad *l*, *m*, *n*, and *k* proton peaks are analogous to those seen in Figure 2c, indicating the presence of residual hexanal after the 120 °C reaction step (expected due to its bp of 130 °C). The absence of water after this step is also consistent with the dehydration of the imine precursor during this elevated temperature synthesis. We note that the NMR tubes and PDA, TPA, and BTA shown in Figures 2a, and 3a,b respectively, were not dried (unlike the other spectra) and therefore contain residual water signals. The spectra also indicate the presence of residual aldehyde species through the appearance of convoluted *a*, *b*, *c*, and *d* proton peaks. Figure 3c also shows the formation of new broad *r* and *q* aromatic peaks as well as the formation of a new broad *p* imine peak that appears at ≈8 ppm, in a similar location to the *j* imine proton peak seen in Figure 2c. When considered in totality, these spectra indicate the formation of branched, dehydrated, macromolecular polyPMI species that still retain some aldehyde species and hexyl-terminated moieties. These results indicate that the imine metathesis reaction is likely reversible to some extent at 120 °C or has not fully completed, which is in accordance with what would be expected for a partially completed step-growth polymerization that is conducted at a temperature slightly below the boiling point of hexanal (130 °C).

To understand the electrochemical behavior of this polyPMI material, cured polymer films (with no added conductive carbon or silicon nanoparticles, optical images shown in Figure S1, Supporting Information) were assembled into coin cells with lithium metal counter electrodes (half-cell configuration). **Figure 4**a shows the cyclic voltammetry (CV) data of a

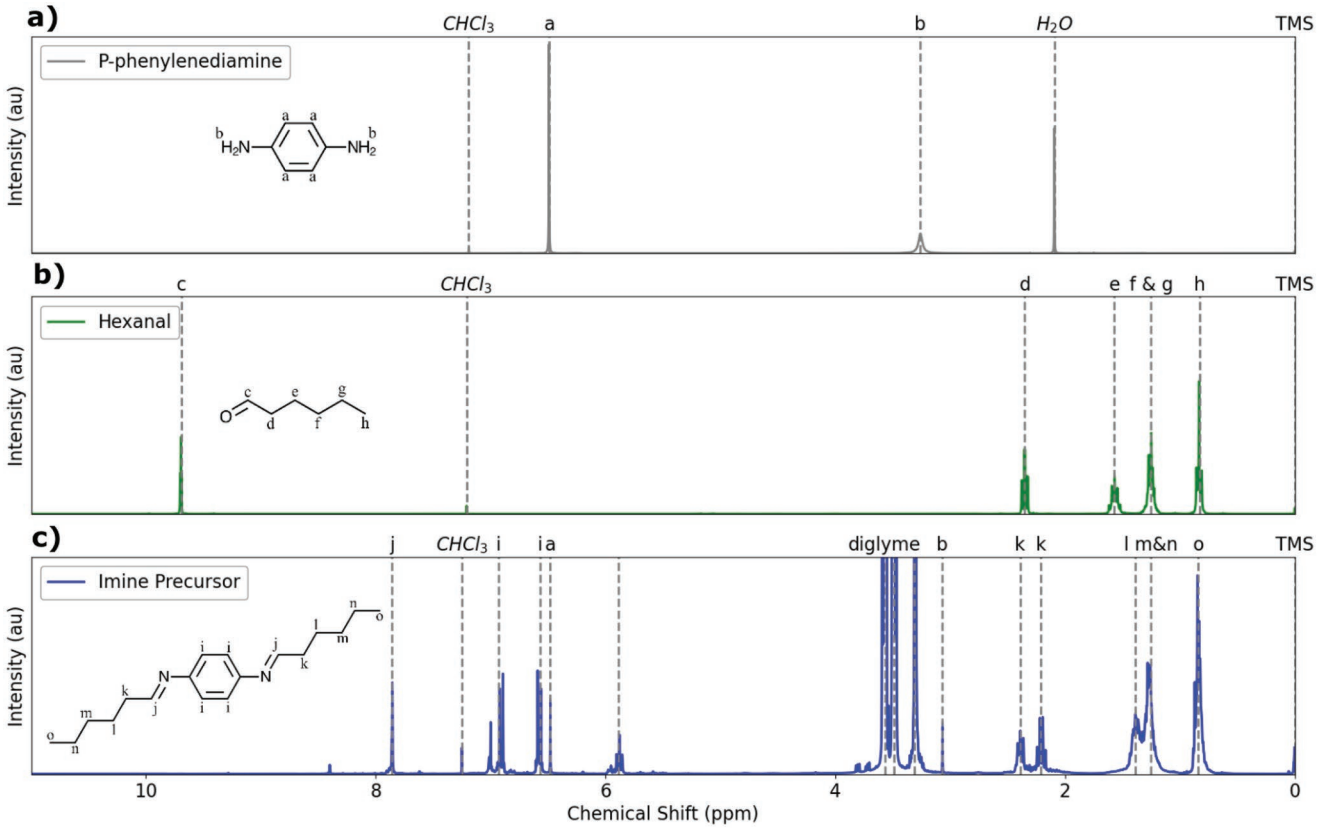

Figure 2. a) ^{1}H NMR spectrum for PDA in $CDCl_3$ solvent. b) ^{1}H NMR spectrum for hexanal in $CDCl_3$ solvent. c) ^{1}H NMR spectrum for imine precursor in diglyme with $CDCl_3$ solvent.

representative polyPMI cell. The cell began with an open circuit voltage (OCV) of ≈2.6 V and was scanned at a rate of 10 mV s^{-1} between 100 mV and 4.5 V. During the first CV scan, the data in Figure 4a show a broad reduction/lithiation peak down to 100 mV, and a subsequent broad oxidation/delithiation peak up to ≈3.7 V. At voltages between 3.7 and 4.5 V, we note the sharp increase in current, which we attribute to the oxidative decomposition of polyPMI above 3.7 V. CV scans were taken at a relatively fast rate of 10 mV s^{-1} to minimize the time spent in this oxidative decomposition regime, to broadly probe the redox activity of the polyPMI, and to determine a suitable voltage stability window. After the first scan, the CV data are relatively consistent, with the emergence of a reductive peak at ≈2.5 V. Figure 4b shows voltage profiles for a representative cell when cycled between 10 mV and 3.0 V for 60 cycles at a slower cycling rate of C/10 and a current density of 6.5 μA cm^{-2} to fully probe the lithiation/delithiation of the polyPMI. The solid curves represent the lithiation profile, the dashed curves represent the delithiation profile, and the specific capacity has been calculated using the mass of the polyPMI film. Each subsequent cycle has been offset by the reversible capacity of the previous cycle, thereby providing a metric to gauge the total amount of lithium held within the polyPMI. The polyPMI electrode initially exhibits incomplete delithiation but begins to cycle semi-reversibly at approximately cycle 40, where the electrode has cumulatively held ≈400 mAh g^{-1} of charge.

Figure 4c plots the discharge (lithiation), charge (delithiation), and Coulombic efficiency (CE) reversible cycling data for the same data presented in Figure 4b. We note that the CE begins to slowly plateau toward the end of cycling, and the cell reversibly cycles with ≈60 mAh g^{-1} specific capacity. Figure 4d shows the dQ/dV plots for the cell, where a broad reductive lithiation peak is seen approaching 10 mV and a broad oxidative delithiation peak is seen from 10 mV to ≈1.5 V at a nominal C/10 rate. These results are aligned with the CV data presented in Figure 4a and further probe the full lithiation/delithiation of the polymer at a slower rate while remaining below the oxidative decomposition regime. We attribute this slow lithiation and activation of the polyPMI to Li^+ coordination at the imine bonds and at the benzene rings of the material. Other reports have used imine COFs to create organic batteries that exhibit similar behavior.[8] We posit that the gradual reaction of the polyPMI with Li^+ leads to improved electronic and ionic conductivities that eventually facilitate stable reversible cycling. Moreover, related studies have demonstrated Li^+ activation in polyaniline-based composite electrodes[31] that is consistent with the reversible lithiation/delithiation electrochemistry observed with polyPMI.

The stable lithiation and delithiation data seen in Figure 4 over a broad electrochemical potential range between 10 mV and 3.7 V, as well as the mechanically flexible nature of the hyperbranched polyPMI, suggests that this new, reversible, oxygen- and water-free polyPMI chemistry could be applied to

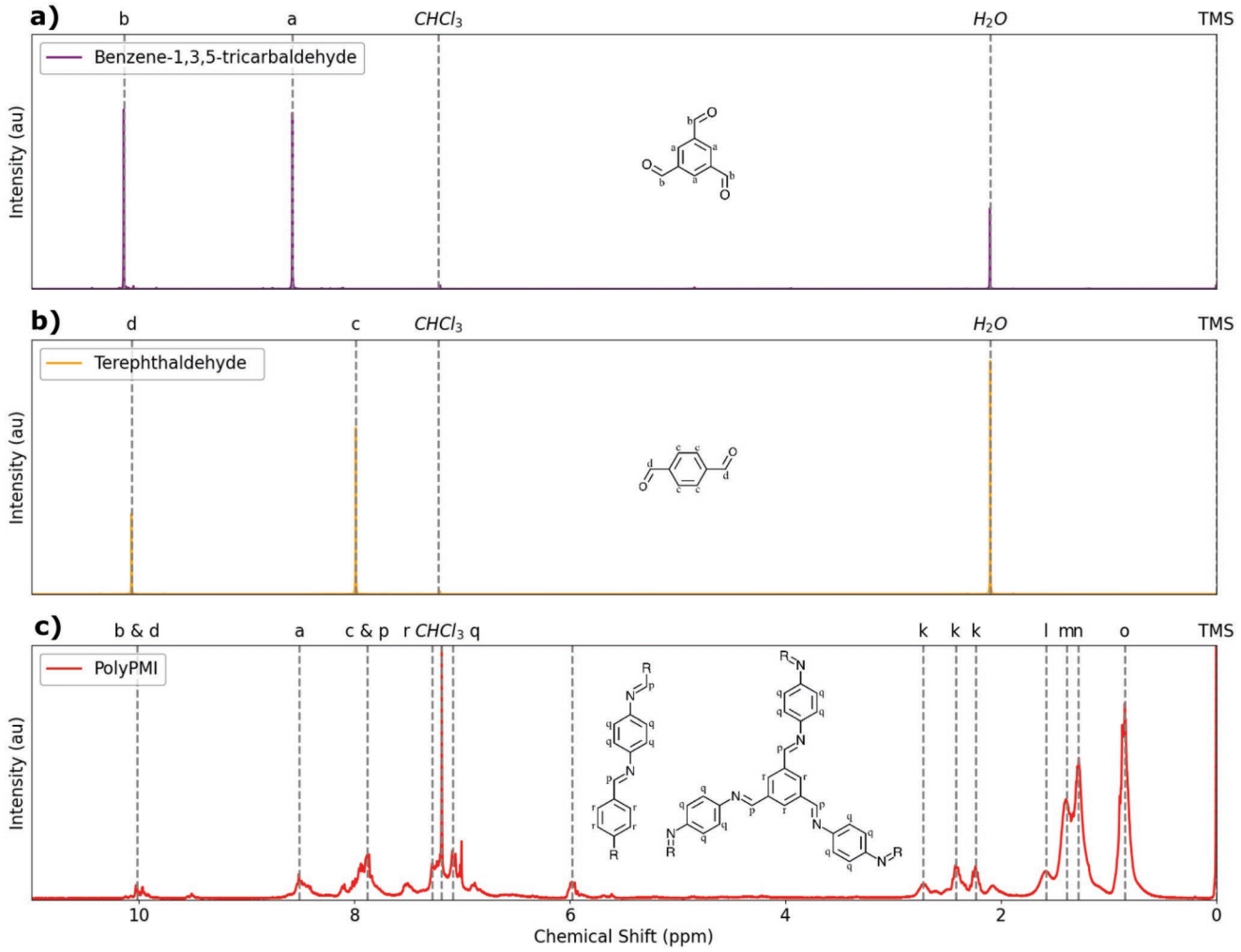

Figure 3. a) ^{1}H NMR spectrum for neat BTA in $CDCl_3$ solvent. b) ^{1}H NMR spectrum for neat TPA in $CDCl_3$ solvent. c) ^{1}H NMR spectrum for polyPMI synthesized at 120 °C for 120 min in diglyme, isolated, and redispersed in $CDCl_3$ solvent.

a range of different technologies such as all-organic batteries, transistors, polymer recycling,[28] OPVs, or LIB conversion electrodes with large volumetric changes during lithiation and delithiation. To demonstrate the utility of this approach, we apply polyPMI as a molecular coating on highly air-reactive silicon nanoparticles (Si NPs) for lithium-ion battery anodes. Our prior work has demonstrated that water will readily oxidize Si NPs produced from plasma-enhanced chemical vapor deposition (PECVD) to produce SiO_2 nanoparticles, the latter of which are electrochemically inactive to lithiation/delithiation.[32] Additionally, we have successfully modified the surface chemistry of PECVD Si NPs by reaction of surface silicon hydrides (*SiH_x) with a variety of organic moieties including alkenes,[33] alcohols,[34,35] amines,[34] aldehydes,[35] amides,[32] and peroxides.[36] Using this radical-based Si NP surface modification chemistry as a starting point, we develop an analogous method to coat 30 nm diameter Si NPs with TPA as shown in **Scheme 2**a. We additionally use the imine metathesis reaction with the trialdehyde precursor BTA discussed previously to grow branched polyPMI oligomers on Si NPs as shown in Scheme 2b. In both cases, these reactions grow from the Si NP surface and cover the Si NPs with conjugated polyamine polymers that we represent schematically in Scheme 2c).

An additional potential benefit of such a polyPMI-coated Si NP (Si@polyPMI) in a high Si-content battery anode is that the flexible, π-conjugated polymeric coating may exhibit mechanical resilience as well as electronic and ionic transport to and from the Si NP surface (**Figure 5**a). Optical images of the Si@polyPMI as well as the branched polyPMI with no Si NPs (Figure 5b) demonstrate that both mixtures are dispersions in diglyme suitable for processing into electrodes. The ^{1}H NMR spectra shown in Figure 3 indicate the need for a higher temperature curing step that will complete the polymerization and that will remove the remaining alkyl and aldehyde containing species to fully form a hyperbranched polyPMI material. To achieve this aim and to fabricate effective Si NP-based anodes, we develop a method to create a printable electrode slurry wherein the Si NPs are coated with branched polyPMI oligomers and the resulting Si@polyPMI NPs are combined with conductive carbon in diglyme. This slurry is subsequently printed on a copper current collector, vacuum dried at 150 °C, transferred to a dry nitrogen tube furnace, and annealed at

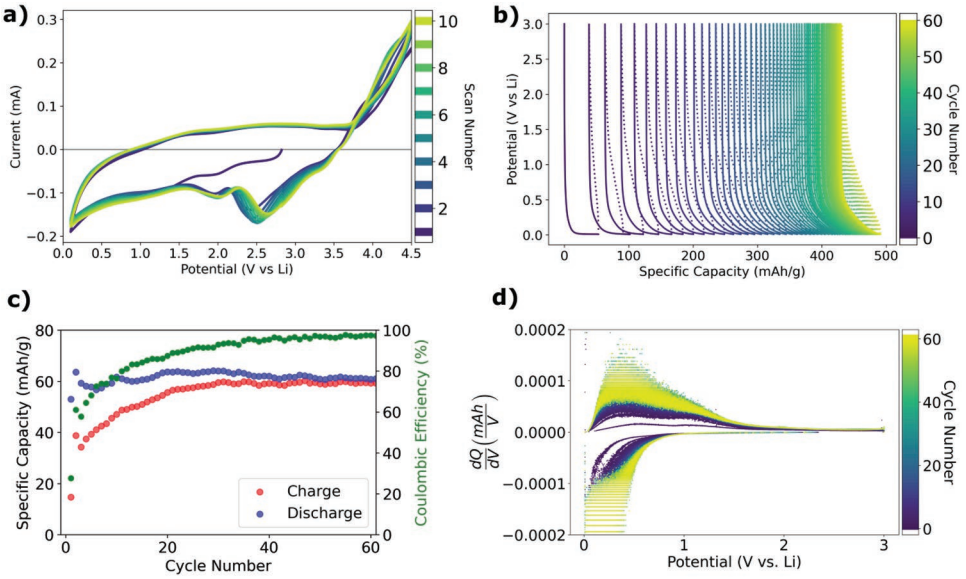

Figure 4. a) Cyclic voltammetry data for a representative polyPMI cell versus a lithium metal counter electrode. b) Voltage profiles for a representative polyPMI cell versus a lithium metal counter electrode for 60 cycles. c) Specific capacity and coulombic efficiency for a representative polyPMI cell versus a lithium metal counter electrode for 60 cycles. d) dQ/dV plots of a representative polyPMI cell versus a lithium metal counter electrode for 60 cycles.

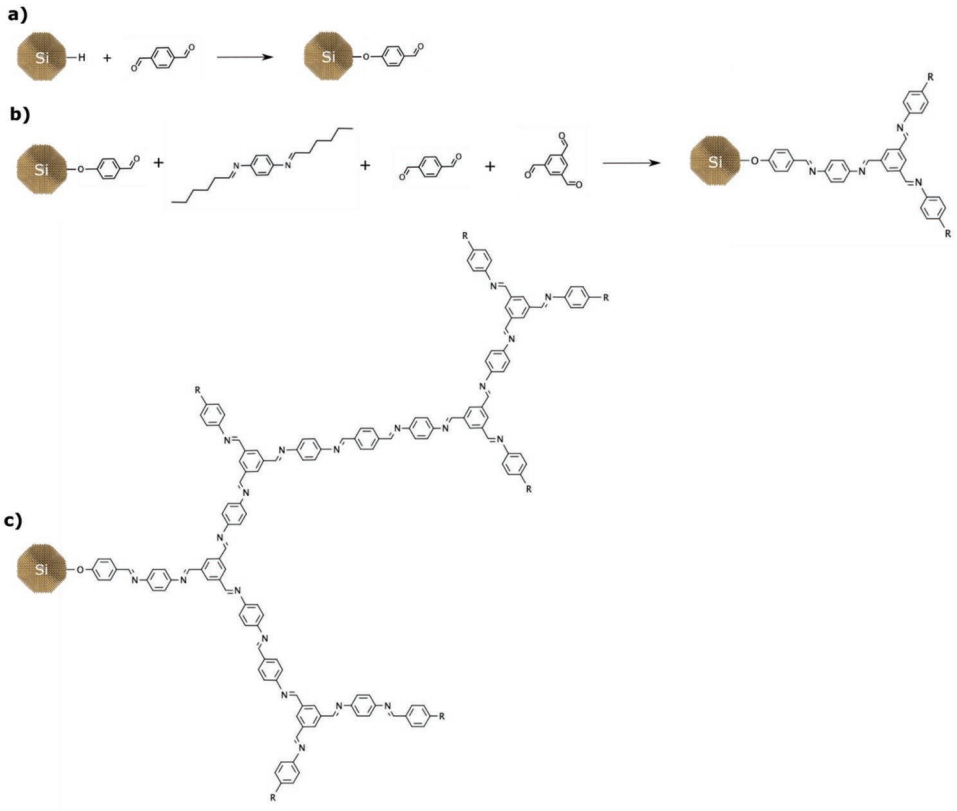

Scheme 2. a) Interaction between a surface silicon hydride (Si–H) on PECVD-grown Si NPs and the dialdehyde TPA to form a silyl-ether moiety at the Si NP surface and leave a reactive phenylaldehyde group. b) Subsequent imine metathesis interaction with the anhydrous hexylamine precursor to form polyPMI oligomers. *R* groups represent any hexyl-terminated moieties, additional polyPMI repeat units, or other molecularly coated Si NPs. c) One representative potential hyperbranched polyPMI oligomer structure prior to final electrode 350 °C curing step.

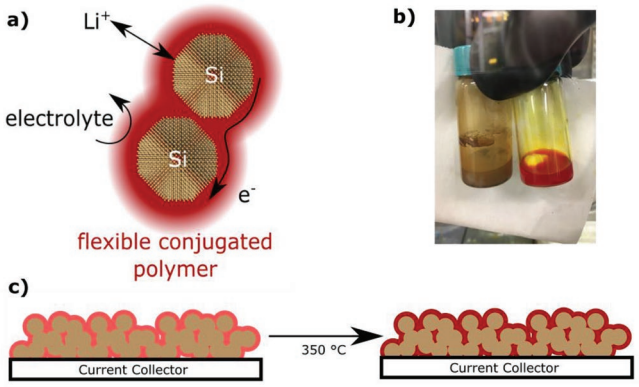

Figure 5. a) An ideal Si NP coating will conduct Li-ions and electrons, block electrolyte side reactions at the NP surface, and accommodate Si volume change during lithiation and delithiation as a flexible coating; a set of material properties for which polyPMI is uniquely well-suited. b) Optical images of Si@polyPMI NPs as depicted in Scheme 2c (left) and hyperbranched polyPMI alone after reacting at 120 °C for 120 min as depicted in Scheme 1c (right). c) Final electrode curing at 350 °C completes the polyPMI polymerization and promotes the formation of larger polyPMI hyperbranched macromolecules.

350 °C for 4 h. We find that this final curing step is necessary to remove any residual hexanal species or alkyl terminating species, fully react the TPA and BTA precursors, and promote the complete polymerization of the polyPMI material as depicted in Figure 5c.

These annealed Si@polyPMI anodes are combined with a lithium metal counter electrode in a half-cell configuration to study their electrochemical performance. The data presented in **Figure 6**a show the specific capacity of the first formation cycles, where the first lithiation (discharge) cycle yields a capacity greater than 1000 mAh g^{-1} and subsequent formation cycles plateau at ≈600 mAh g^{-1}. The data presented in Figure 4 are collected at a relatively low current density of 6.5 μA cm^{-2} due to the slow kinetics of the bulk polyPMI film without any additional conductive additives. The data presented in Figure 6, however, are collected at a current density of ≈450 μA cm^{-2} to target a 1 C cycling rate. Therefore, we conclude that the capacity contribution of the polyPMI is minimal in comparison to the Si NP active material contribution when combined into a composite anode. Importantly, we highlight that the coulombic efficiency of the cells exceeds 90% after the first cycle and exceeds 99.5% after the 10th cycle, indicating a high degree of interfacial passivation for the high surface area 30 nm diameter Si NPs. The data shown in Figure 6b show the reversible capacity for the half-cell Si@polyPMI anodes for 250 cycles, where the capacity fade is minimal, and the coulombic efficiency remains well above 99.5% for the duration of the test. Figure 6c shows the same cycling data scaled to areal loading with an additional calculated accumulated irreversible capacity (AIC) curve to represent the Li^+ consumption of the half-cell after the formation cycles when an effectively unlimited Li^+ source is present, which is calculated by the cumulative sum of the difference between lithiation and delithiation capacities over 250 cycles (analogous to the voltage profile offsets seen in Figure 4b). Figure 6d shows the differential capacity versus voltage (dQ/dV) plots for the cycling data, which exhibit the characteristic lithiation and delithiation peaks of similar Si NP systems described previously in our other work.[32,37]

These annealed Si@polyPMI anodes were also used to fabricate full-cells with a $LiFePO_4$ (LFP) cathode without a prelithiation step by using a higher loading LFP cathode with excess Li^+ inventory. LFP was chosen due to its relatively flat

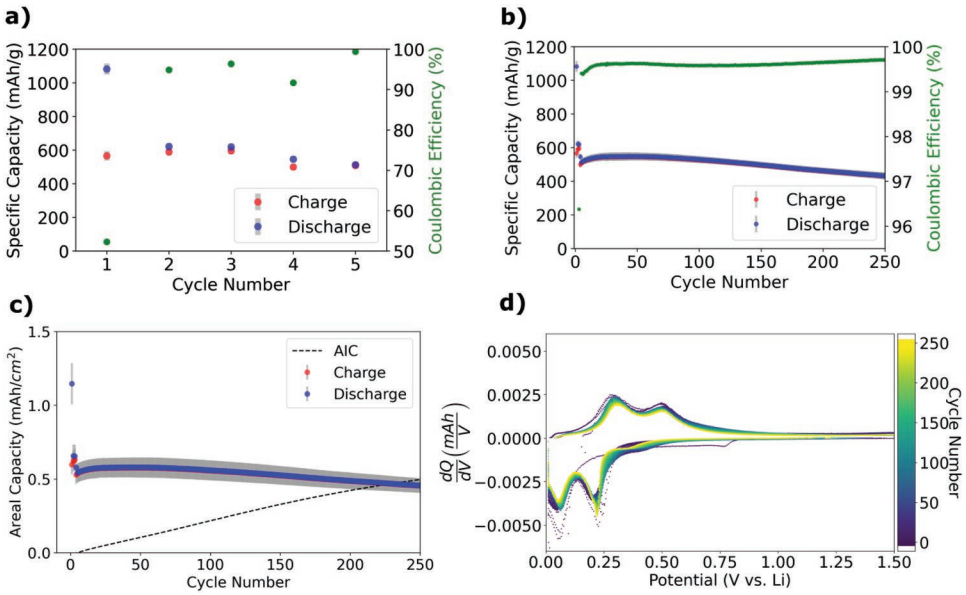

Figure 6. a) Mean Si@polyPMI NP anode half-cell specific capacity and coulombic efficiency for the first five cycles, including the first three formation cycles (C/20) for triplicate cells with grey error bars. b) Si@polyPMI NP anode half-cell specific capacity and coulombic efficiency for 250 cycles at a nominal rate of 1 C. Data are presented as the mean of triplicate cells with grey error bars representing one standard deviation. c) Si@polyPMI NP anode half-cell areal capacity and the calculated accumulated irreversible capacity (AIC). Data are presented as the mean of triplicate cells with grey error bars representing one standard deviation. d) dQ/dV plots of a representative Si@polyPMI NP half-cell for 250 cycles.

voltage profile such that the performance of the Si@polyPMI anode could be assessed independent of cathode effects. The data presented in **Figure 7**a show the specific capacity of the first formation cycles and Figure 7b shows the subsequent reversible capacity of a representative full-cell for 500 cycles at a relatively fast rate of 1 C. It is clear that the reversible cycling capacity of the full-cell in Figure 7b is lower compared to that of the half-cell in Figure 6b. We attribute this difference to the significant loss of Li^+ inventory in the higher loading LFP cathode during the first cycle, which will reduce the effective electrochemical potential window in the cell and lead to incomplete lithiation and delithiation during cycling. Impressively, the coulombic efficiency increases above 99.9% within the first few cycles and eventually plateaus above 99.95% during subsequent cycles, indicating a high degree of interfacial passivation of the Si NPs by the polyPMI coating.

Detailed electrochemical characterization was conducted every 100 cycles using a hybrid pulse power characterization (HPPC) method to determine the area specific impedance (ASI) (Figure S2, Supporting Information), which is found to increase only very slightly; from ≈26 to 28 Ω cm^{-2} after 400 cycles. The cells were also cycled at a rate of C/3 every 100 cycles to evaluate the rate capability of the cells, where the slower C/3 cycling rate yields a slightly higher reversible capacity (Figure 7c). Figure 7d shows a representative dQ/dV plot for the cell. The electrochemical data in Figures 6 and 7 indicate a highly stable Si@polyPMI anode and demonstrate that this novel polyPMI chemistry can be effectively used to passivate Si NPs used in LIB conversion electrodes.

Interestingly, especially in the half-cell configuration, the first cycle of the cell yields a relatively high discharge capacity, however subsequent cycles yield significantly lower capacities. Moreover, the ultimate specific capacity values remain well below what can hypothetically be achieved with a high silicon content (60% by mass silicon yields a maximum specific capacity of 2100 mAh g^{-1}) electrode. We also tested electrodes that were calendered after the first drying step and then subsequently annealed in a tube furnace as depicted in **Figure 8**a. Figure 8b compares the reversible cycling performance of these calendered cells in comparison to the uncalendered cells from Figure 6b. Figure 8c shows an image of the calendered electrodes with a relatively glossy and flat top surface. Interestingly, the calendered electrodes do not exhibit the expected increased cycling capacity due to improved conduction pathways, and instead show a gradual increase in reversible capacity over the course of 100 cycles. We attribute this result to the low porosity of the calendered electrodes, which will result in slow electrolyte wetting over time and the observed gradual increase in specific capacity over many cycles. Therefore, we hypothesize that the observed lower than expected reversible capacity is due to a loss of porosity from initial solid electrolyte interphase (SEI) formation, where some portion of the pores in the electrode are effectively sealed off from electrolyte access that limits bulk ionic transport within the anode after the first cycle. We conclude that the limiting factor of these electrodes is porosity and not electrical conductivity, ionic conductivity, surface passivation, or interconnectedness of the polyPMI material. To probe this hypothesis, we fabricate a set of uncalendered silicon anodes using smaller 3.7 nm diameter silicon nanoparticles with no added conductive carbon in the slurry mixture, where all other experiments are conducted with the larger and therefore more porous 30 nm diameter particles. The data shown in Figure 8d demonstrate that these cells exhibit similar reversible capacities and comparably high coulombic efficiencies to electrodes with

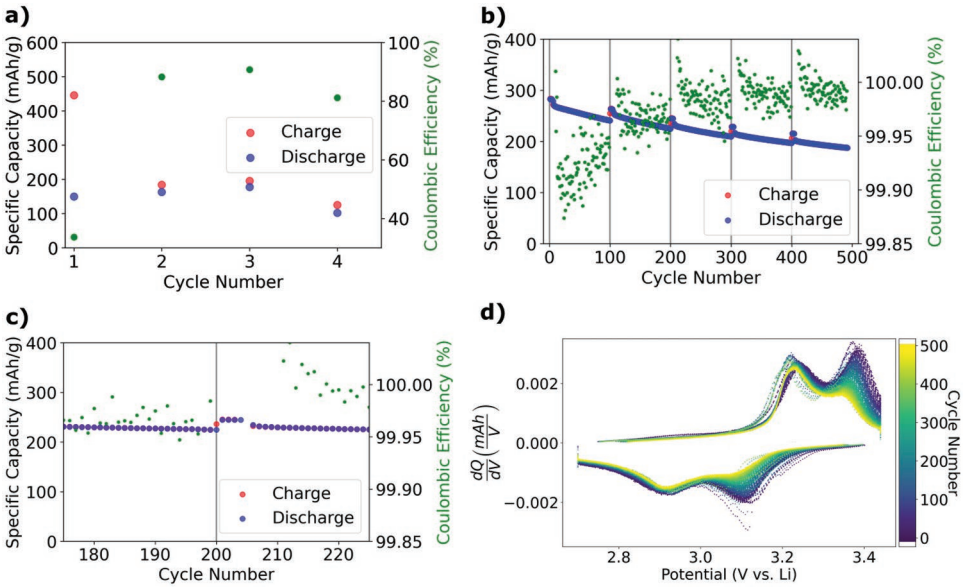

Figure 7. a) Representative Si NP anode paired with an LFP cathode as a full cell with anode specific capacity and coulombic efficiency for the first C/20 formation cycles. b) Representative Si NP anode paired with an LFP cathode as a full cell with anode specific capacity and coulombic efficiency for 500 cycles at a nominal 1 C cycling rate with 4× cycles at a nominal C/3 cycling rate and HPPC pulses every 100 cycles (locations indicated with vertical grey lines). HPPC time constant results are shown in Figure S2, Supporting Information and data normalized to the cathode mass are presented in Figure S3, Supporting Information. c) Zoomed in plot showing the specific capacity change during the slower C/20 cycles near cycle 200 for a representative Si NP anode. d) dQ/dV plots for a representative Si NP full cell for 500 cycles.

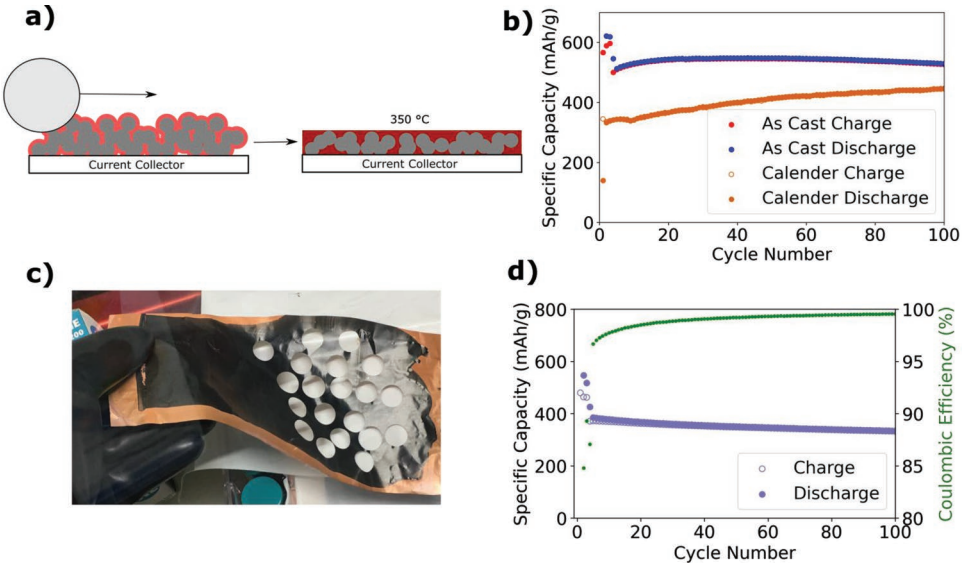

Figure 8. a) Diagram depicting electrodes where the as cast electrode with polyPMI oligomers is calendered and then subsequently annealed in an inert atmosphere. b) Si NP anode half-cell specific capacity for 100 cycles at a nominal rate of 1 C for the baseline uncalendered (as cast) cells shown in Figure 5b compared to calendered cells. Data are presented as the mean of triplicate cells. c) Image of calendered electrode sheet. d) Si NP anode half-cell specific capacity and coulombic efficiency for 100 cycles at a nominal rate of 1 C for triplicate cells made using 3.7 nm Si@polyPMI NPs and no added conductive carbon. Data are presented as the mean of triplicate cells.

substantial amounts (10 wt%) conductive carbon (Figure 6b). These results conclusively establish that polyPMI is an effective electronic and ionic conductor that provides exceptional Si surface passivation.

To better understand why polyPMI provides such a robust Si coating, we also examine the annealed electrode material using transmission electron microscopy (TEM) as shown in **Figure 9**. The images show that the 30 nm diameter Si NPs are completely covered with a non-porous polymeric coating. Combined with energy-dispersive X-ray spectroscopy (EDS) data and elemental mapping (Figures S4 and S5, Supporting Information), these data suggest that polyPMI both isolates the Si NP surface from direct contact with electrolyte as well as mitigates Si electrical isolation during lithiation/delithiation as significant volume expansion/contraction occurs.

Finally, we examine the macroscopic electrode morphology and chemical composition ex situ using scanning electron microscopy (**Figure 10**) and EDS mapping (Figures S6–S12, Supporting Information). Figure 10a and Figure S6, Supporting Information, show that after calendaring and curing, the electrodes have low porosities and are relatively uniform and homogenous with small nanoscale surface features. Once the cells have undergone the formation cycles, the surface of the macroscopic electrodes are coated with larger SEI grains (Figure 10b). Surprisingly, after cycling for 200 cycles (electrochemical data, Figure S13, Supporting Information), this initial SEI morphology remains unchanged (SEM, Figure 10c), further corroborating the high electrochemical and mechanical stability achieved with this novel polyPMI material. Moreover, the electrodes do not show any evidence of cracking, delamination, or other mechanical failure after cycling, thereby corroborating our hypothesis that the polyPMI provides a robust flexible coating that can accommodate many cycles of Si NP expansion and contraction. The excellent mechanical stability of the polyPMI is also enhanced by its strong adhesion to the copper current collector surface after curing, as shown in Figure S1, Supporting Information. X-ray photoelectron spectroscopy (XPS) shown in Figure S14 and Table S1, Supporting Information, indicate the formation of a significant amount of lithium fluoride as well as lithium-carbonate type species within the

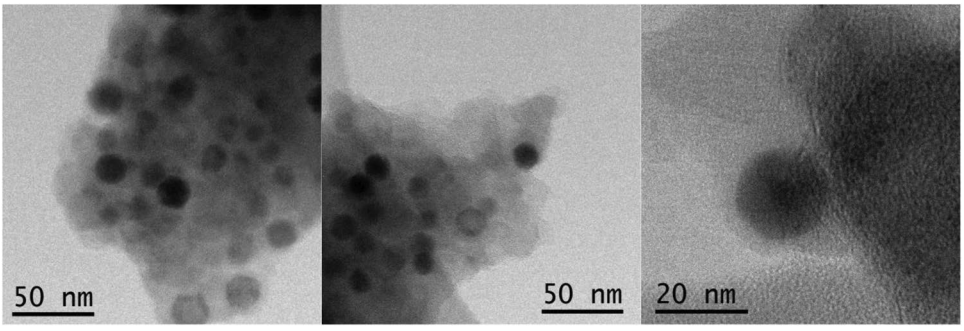

Figure 9. TEM images of Si NPs coated with hyperbranched polyPMI after 350 °C curing.

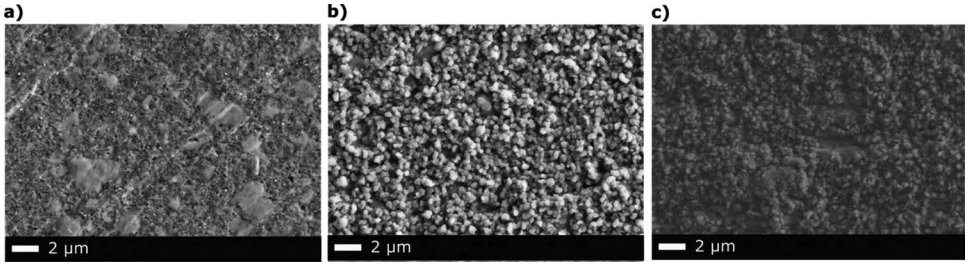

Figure 10. SEM image of pristine 30 nm Si@polyPMI electrodes with conductive carbon a) after calendaring and final 350 °C curing, b) after the initial formation cycles, and c) after 200 cycles in a half cell configuration.

SEI, in line with previous reports of similar SEI species corresponding to stable electrode cycling.[38–42] Extended cycling results in more lithium carbonate and lithium alkyl carbonate deposition on top of the LiF-rich SEI, with LiF remaining a major SEI component after formation and extended cycling.

3. Conclusions

We have demonstrated a new, simple step-growth method for using alkylimine-based metathesis to make polyamines relevant for a range of different technologies such as all-organic batteries, transistors, polymer recycling, OPVs, or LIB applications. We showed that this new imine metathesis reaction can be used to form both linear and branched π-conjugated polyphenylmethanimine (polyPMI) based polymers. As an example of this new method's utility, we showed that hyperbranched polyPMI oligomers can be grown on silicon nanoparticles to create an ionically and electronically conductive coating that effectively passivates the silicon in a liquid electrolyte LIB. When used as oligomeric coatings on silicon nanoparticles, complete polymerization is achieved during an electrode curing step. By leveraging this chemistry, we fabricated highly stable silicon anodes in a full-cell LIB configuration against lithium iron phosphate cathodes achieving greater than 99.95% coulombic efficiency after the first 100 cycles. This new synthetic method is broadly applicable to a variety of air- and water-sensitive materials, which were previously incompatible with conjugated imines synthesized via conventional polycondensation.

4. Experimental Section

Conventional One-Step Polycondensation of Linear Polyamines: All reagents were purchased from Sigma Aldrich unless otherwise noted. All reactions and electrode fabrication steps were conducted in an inert argon atmosphere glovebox (H_2O < 1.0 ppm and O_2 < 1.0 ppm) unless otherwise noted. Phenylenediamine (PDA, 0.1 mmol, 10.8 mg), purified by drying in a vacuum desiccator for 24 h, was transferred to a glovebox under an argon atmosphere and dissolved in 1.5 mL anhydrous diglyme. Terephalaldehyde (TPA, 0.1 mmol, 13.4 mg) was dried in a vacuum desiccator for 24 h, transferred to a glovebox under an argon atmosphere and dissolved in 1.5 mL anhydrous diglyme. Both mixtures were combined and heated to 120 °C for 60 min resulting in an orange-colored suspension.

Imine Precursor Solution Synthesis: Dried PDA (5.0 mmol, 541 mg) was dissolved in 8.3 mL anhydrous diglyme. Hexylaldehyde (10.0 mmol, 1.2 mL) was injected into the solution and the mixture was heated to 100 °C for 60 min to complete the reaction and to dehydrate the solution (with continued sparging). This imine precursor solution (0.5 mmol mL^{-1}) was cooled to ambient temperature and transferred back into a glovebox.

Two-Step Imine Metathesis to form Linear Polyamines: Dried TPA (0.1 mmol, 13.4 mg) was dissolved in 2.8 mL of anhydrous diglyme and 0.2 mL of the imine precursor was added to the solution. The mixture was heated to 120 °C for 60 min and a dark, red-colored solution was produced.

Two-Step Imine Metathesis to form Hyperbranched Polyamines: Dried benzene-1,3,5-tricarboxaldehyde (BTA, 0.03 mmol, 5 mg) and TPA (0.09 mmol, 12 mg) were dissolved in 2.8 mL of anhydrous diglyme and 0.24 mL of the imine precursor solution was added to the mixture. The mixture was heated to 120 °C for 60 min and a dark red-colored suspension was produced.

Absorbance Spectroscopy: All absorbance (UV–vis) measurements were conducted in an argon-filled glove box at ambient temperature using a sealed quartz cuvette and a fiber optic coupling to an external source and detection system through an F25 fiber-coupling flange mounted on the side of the glovebox. The light source was a Thorlabs M405FP1 fiber-coupled LED using a Thorlabs DC2200 LED driver as the power source. The UV–vis (l = 300–900 nm) and NIR (l = 900–2200 nm) spectra were collected simultaneously through a bifurcated fiber cable, which was oriented in direct transmission through the sample from the source. An Ocean Optics OceanFX UV–vis spectrometer and an Ocean Optics NIRQuest NIR spectrometer were used to record the UV–vis and NIR spectra, respectively. To ensure accurate measurements, the spectrometer photoresponse was calibrated against a 3000 K tungsten–halogen blackbody source (Ocean Optics HL-2000-HP).

Density Functional Theory Calculations: Predicted absorbance spectra (oscillator strengths), electron orbitals, energy states, and natural transition orbitals (NTOs) were calculated using the Amsterdam density functional (ADF2019.303) software for linear polyPMI oligomers of several lengths.[43,44]

^{1}H Nuclear Magnetic ResonanceSpectroscopy: All samples were tested in $CDCl_3$ solvent at a 20 mg mL^{-1} concentration. ^{1}H NMR spectra were acquired at 25 °C on a Bruker Avance NeoNanobay 300 MHz spectrometer at 7.05 T using a room temperature broadband probe. Spectra were acquired with a spectral width of 14 ppm with a recycle delay of 1 s and 8 scans. All spectral processing was done in Bruker Topspin version 3.6.1. TPA, PDA, BTA, and hexylaldehyde were used as received without drying or further purification for initial spectra. NMR tubes were dried overnight in an oven at 100 °C prior to use, expect in the case of the TPA, PDA, and BTA where the NMR tubes were not dried because of the presence of water in these reagents prior to dehydration.

PolyPMI Electrode Fabrication: Dried BTA (20 mg) and TPA (48 mg) were dissolved in 2.0 mL anhydrous diglyme and 0.96 mL of the imine precursor was added to the solution. The solution was briefly vortex mixed and sonicated and was drop cast onto a copper foil current collector (total reaction time before drop-casting was ≈15 min). The electrodes were subsequently dried under vacuum at 150 °C for 4 h. The resulting bright red electrode layer was punched into 14 mm diameter punches that were subsequently cured at 500 °C in a nitrogen purged tube furnace for 4 h, producing a dark purple-colored electrode.

Anode Fabrication using 30 nm Silicon Nanoparticles: Dried TPA (2.1 g) was melted in a 20 mL scintillation vial at 125 °C and 300 mg of silicon

nanoparticles (Si NPs) produced from plasma-enhanced chemical vapor deposition (PECVD) with hydrogen-termination and an approximate diameter of 30 nm (see our previous works[32–34,37] and supporting information for details) were added to the melted TPA. The mixture was stirred for 4 h at 125 °C and then cooled to ambient temperature. The resulting solid mixture of coated Si NPs and extra TPA was washed in 10 mL of anhydrous toluene and was centrifuged at 12 000× *g* for 5 min. The toluene wash was separated by decanting, and the process was repeated two additional times (three times total) to complete the washing procedure. The resulting Si@TPA NPs were dried under vacuum for 1 h.

To make Si@polyPMI, 180 mg of the Si@TPA NPs were added to 1 mL of anhydrous diglyme and BTA (0.06 mmol, 10 mg), TPA (0.18 mmol, 24 mg), and 0.48 mL (0.24 mmol) of the imine precursor solution was added to the mixture. The mixture was heated at 125 °C for 30 min, cooled to ambient temperature, followed by brief vortex mixing and sonication to ensure adequate dispersion.

To make final electrodes, 60 mg of Timcal C65 conductive carbon was added to the mixture to form a printable slurry (mass ratios: 60% Si, 20% polyPMI, 20% Timcal C65). Each slurry was then mixed for 90 s using a planetary mixer (Mazerustar KK-250S planetary mixer, setting 13) before being cast onto a Cu foil using a blade casting coater with a wet gap of 250 µm and a casting speed of ≈1 cm s^{-1}. The electrodes were subsequently cured under vacuum at 150 °C for 4 h. Next, the dried electrodes were punched into 14 and 15 mm diameter punches and were cured at 350 °C in a nitrogen purged tube furnace for 4 h. The final electrodes had mass loadings of 1.06 ± 0.16 mg cm^{-2} (total composite electrode mass).

Half Cell Fabrication: The electrodes were tested using 2032 coin cells in the half-cell configuration. Each electrode was tested multiple times, using 3 identical cells with 14 mm-diameter circular punches from each electrode. The half-cells were assembled in a glovebox with the 14 mm silicon electrodes as the positive electrode. The negative electrodes used were 9/16 inch diameter circular punches of Li metal foil (Alfa Aesar 10 769, 0.75 mm thick, 99.9% metals basis) that were cleaned with a toothbrush before being pressed onto a 15 mm-diameter, 1 mm-thick stainless-steel spacer with a stainless-steel wave spring positioned on the opposite side. The electrodes were separated by a 19 mm circular punch of porous polypropylene separator (Celgard 2325). Each cell was injected with 20 µL of the Gen2F electrolyte ($LiPF_6$ in ethylene-carbonate/ethyl-methyl-carbonate in a 3:7 by mass ratio with 3 wt% of fluoroethylene carbonate added) onto each side of the separator (40 µL total) before the cells were sealed by a hydraulic crimper. Each cell was allowed to rest at open circuit potential for 4 h before being galvanostatically cycled between 0.01 and 1.5 V versus Li at C/20 forming cycles followed by cycling at 1 C.

Full Cell Fabrication: $LiFePO_4$ (LFP) cathode full-cells were assembled in an analogous manner to the half-cells, with a few differences. Specifically, the 2032 coin cells were assembled with a 15 mm diameter silicon anode as the negative electrode on a 0.5 mm-thick stainless steel spacer. The anode was then covered with 40 µL of the Gen2F electrolyte and a 19 mm circular punch of porous separator. A 14 mm diameter circular punch of 1.8 mAh cm^{-2} LFP cathode was placed on top of the separator along with an additional 0.5 mm stainless steel spacer, a wave spring, and the positive electrode cover. The 1.15 mAh cm^{-2} first cycle lithiation capacity of the silicon anodes in a half cell configuration with the 1.8 mAh cm^{-2} LFP cathode gives an N:P ratio ≈0.64. The cell was finally sealed in a hydraulic crimper. Each cell was allowed to rest at open circuit potential for 4 h before being galvanostatically cycled between 2.70 and 3.44 V at C/20 forming cycles followed by cycling at 1 C.

Calendered Silicon Anodes: After vacuum drying, the silicon anodes were removed from the glovebox atmosphere, calendered in a roll press in ambient atmosphere, and transferred back into the glovebox. The electrodes were then punched into 14 mm diameter circular punches and were subsequently cured and assembled into half-cells.

Anodes with 3.7 nm Silicon Nanoparticles and no Conductive Carbon: 3.7 nm diameter Si@polyPMI was synthesized in an analogous manner to the 30 nm particles. The Si@polyPMI nanoparticles were processed into electrodes in the same manner as the 30 nm particles, except no Timcal C65 conductive carbon was added to the slurry mixture. The electrodes were subsequently dried under vacuum, cured, and assembled into half-cells.

Scanning Electron Microscopy (SEM): Cycled electrodes were disassembled from coin cells and rinsed with 675 µL of dimethyl carbonate (DMC) three times to remove any residual electrolyte and dried in an argon glove box before any further ex situ analysis. Electrode morphology was examined using an ex situ field-emission scanning electron microscope (Zeiss Sigma VP) equipped with energy dispersive X-ray spectroscopy (Oxford Instruments) (EDS) at 20 00 kV.

X-Ray Photoelectron Spectroscopy: 30 nm Si@polyPMI electrodes after calendaring and final curing were transferred from an argon glovebox to the XPS chamber using a vacuum-sealed transfer module (Thermo) with no air exposure. Ex situ X-ray photoelectron spectroscopy (XPS) (K-alpha, Thermo) was performed on the samples using an Al Kα X-ray source with a measured spot size of 400 µm and pass energy of 50 eV. Binding energies were corrected based on the hydrocarbon C1s peak at 284.8 eV.

Transmission Electron Microscopy Characterization: The particle morphology and elemental distribution were analyzed using transmission electron microscopy by scraping material from 30 nm Si@polyPMI electrodes after calendaring and final curing. A 300 kV FEI Titan monochromated scanning TEM equipped with a probe aberration corrector was used to acquire the TEM images. Uncycled anodes were scraped with a razor blade, polished between glass slides, loaded on a TEM grid, and imaged under low dose conditions. The electron dose rate was ≈1 e $Å^{-2}$ s^{-1} for low mag imaging and ≈100 e $Å^{-2}$ s^{-1} for high resolution TEM imaging to prevent beam induced damage and artifact. Energy dispersive X-ray spectroscopy (EDS) elemental mapping was collected by scanning the same region with multiple times at a dwell time of 0.001–0.01 ms with the electron dose rate of ≈0.363–1.98 e $Å^{-2}$ s^{-1}. The function of binning and the smooth in Aztec software (Oxford Instruments) were used to enhance the contrast of EDS data.

Supporting Information

Supporting Information is available from the Wiley Online Library or from the author.

Acknowledgements

This work was authored in part by the National Renewable Energy Laboratory (NREL), operated by Alliance for Sustainable Energy, LLC, for the U.S. Department of Energy (DOE) under Contract No. DE-AC36-08GO28308. Funding provided by the U.S. Department of Energy's Vehicle Technologies Office (VTO) under the Silicon Consortium Project directed by Brian Cunningham and managed by Anthony Burrell. Project conception, chemical synthesis, LIB fabrication and characterization were conducted at NREL. TEM and EDS mapping data were conducted at PNNL. SEM, EDS mapping, and XPS data were collected and analyzed at URI. The LFP electrode used in this manuscript are from Argonne's Cell Analysis, Modeling and Prototyping (CAMP) Facility, which is fully supported by the DOE VTO. The views expressed in the article do not necessarily represent the views of the DOE or the U.S. Government. The U.S. Government retains and the publisher, by accepting the article for publication, acknowledges that the U.S. Government retains a nonexclusive, paid-up, irrevocable, worldwide license to publish or reproduce the published form of this work, or allow others to do so, for U.S. Government purposes.

Conflict of Interest

The authors declare no conflict of interest.

Data Availability Statement

The data that support the findings of this study are available from the corresponding author upon reasonable request.

Keywords

conjugated polymers, lithium-ion batteries, nanoparticles, silicon anodes

Received: November 17, 2022
Revised: January 10, 2023
Published online: February 17, 2023

[1] O. Inganäs, *Adv. Mater.* **2018**, *30*, 1800388.
[2] H. Jia, T. Lei, *J. Mater. Chem. C* **2019**, *7*, 12809.
[3] S. J. Uke, S. P. Mardikar, A. Kumar, Y. Kumar, M. Gupta, Y. Kumar, *R. Soc. Open Sci.* **2021**, *8*, 210567.
[4] J. Xie, P. Gu, Q. Zhang, *ACS Energy Lett.* **2017**, *2*, 1985.
[5] P. O. Morin, T. Bura, M. Leclerc, *Mater. Horiz.* **2016**, *3*, 11.
[6] T. P. Osedach, T. L. Andrew, V. Bulović, *Energy Environ. Sci.* **2013**, *6*, 711.
[7] T. Bura, S. Beaupré, M. A. Légaré, J. Quinn, E. Rochette, J. T. Blaskovits, F. G. Fontaine, A. Pron, Y. Li, M. Leclerc, *Chem. Sci.* **2017**, *8*, 3913.
[8] Z. Lei, Q. Yang, Y. Xu, S. Guo, W. Sun, H. Liu, L. P. Lv, Y. Zhang, Y. Wang, *Nat. Commun.* **2018**, *9*, 576.
[9] S. Y. Jiang, S. X. Gan, X. Zhang, H. Li, Q. Y. Qi, F. Z. Cui, J. Lu, X. Zhao, *J. Am. Chem. Soc.* **2019**, *141*, 14981.
[10] Y. Hu, N. Dunlap, S. Wan, S. Lu, S. Huang, I. Sellinger, M. Ortiz, Y. Jin, S. H. Lee, W. Zhang, *J. Am. Chem. Soc.* **2019**, *141*, 7518.
[11] E. Vitaku, W. R. Dichtel, *J. Am. Chem. Soc.* **2017**, *139*, 12911.
[12] S. Dalapati, M. Addicoat, S. Jin, T. Sakurai, J. Gao, H. Xu, S. Irle, S. Seki, D. Jiang, *Nat. Commun.* **2015**, *6*, 7786.
[13] J. Guo, Y. Xu, S. Jin, L. Chen, T. Kaji, Y. Honsho, M. A. Addicoat, J. Kim, A. Saeki, H. Ihee, S. Seki, S. Irle, M. Hiramoto, J. Gao, D. Jiang, *Nat. Commun.* **2013**, *4*, 2736.
[14] L. Ascherl, E. W. Evans, M. Hennemann, D. Di Nuzzo, A. G. Hufnagel, M. Beetz, R. H. Friend, T. Clark, T. Bein, F. Auras, *Nat. Commun.* **2018**, *9*, 3802.
[15] C. Yang, S. A. Jenekhe, *Macromolecules* **1995**, *28*, 1180.
[16] L. Wei, C. Chen, Z. Hou, H. Wei, *Sci. Rep.* **2016**, *6*, 19583.
[17] Y. Park, S. Lee, S. H. Kim, B. Y. Jang, J. S. Kim, S. M. Oh, J. Y. Kim, N. S. Choi, K. T. Lee, B. S. Kim, *RSC Adv.* **2013**, *3*, 12625.
[18] J. He, L. Zhang, *J. Alloys Compd.* **2018**, *763*, 228.
[19] C. Li, T. Shi, H. Yoshitake, H. Wang, *J. Mater. Chem. A* **2016**, *4*, 16982.
[20] Z. Liu, S. Han, C. Xu, Y. Luo, N. Peng, C. Qin, M. Zhou, W. Wang, L. Chen, S. Okada, *RSC Adv.* **2016**, *6*, 68371.
[21] L. Zhang, L. Zhang, L. Chai, P. Xue, W. Hao, H. Zheng, *J. Mater. Chem. A* **2014**, *2*, 19036.
[22] W. F. Ren, J. B. Le, J. T. Li, Y. Y. Hu, S. Y. Pan, L. Deng, Y. Zhou, L. Huang, S. G. Sun, *ACS Appl. Mater. Interfaces* **2021**, *13*, 639.
[23] C. Chen, F. Chen, L. Liu, J. Zhao, F. Wang, *Electrochim. Acta* **2019**, *326*, 134964.
[24] D. M. Piper, T. A. Yersak, S. B. Son, S. C. Kim, C. S. Kang, K. H. Oh, C. Ban, A. C. Dillon, S. H. Lee, *Adv. Energy Mater.* **2013**, *3*, 697.
[25] S. Gao, F. Sun, A. Brady, Y. Pan, A. Erwin, D. Yang, V. Tsukruk, A. G. Stack, T. Saito, H. Yang, P. F. Cao, *Nano Energy* **2020**, *73*, 104804.
[26] T. M. Higgins, S. H. Park, P. J. King, C. Zhang, N. McEvoy, N. C. Berner, D. Daly, A. Shmeliov, U. Khan, G. Duesberg, V. Nicolosi, J. N. Coleman, *ACS Nano* **2016**, *10*, 3702.
[27] Y. H. Choi, H. Park, S. Lee, H. D. Jeong, *ACS Omega* **2020**, *5*, 8629.
[28] T. Lei, X. Chen, G. Pitner, H. S. P. Wong, Z. Bao, *J. Am. Chem. Soc.* **2016**, *138*, 802.
[29] T. Xiang, X. Liu, P. Yi, M. Guo, Y. Chen, C. Wesdemiotis, J. Xu, Y. Pang, *Polym. Int.* **2013**, *62*, 1517.
[30] D. Sek, A. Iwan, B. Jarzabek, B. Kaczmarczyk, J. Kasperczyk, Z. Mazurak, M. Domanski, K. Karon, M. Lapkowski, *Macromolecules* **2008**, *41*, 6653.
[31] A. B. Puthirath, B. John, C. Gouri, S. Jayalekshmi, *RSC Adv.* **2015**, *5*, 69220.
[32] G. M. Carroll, M. C. Schulze, T. R. Martin, G. F. Pach, J. E. Coyle, G. Teeter, N. R. Neale, *ACS Appl. Energy Mater.* **2020**, *3*, 10993.
[33] L. M. Wheeler, N. C. Anderson, P. K. B. Palomaki, J. L. Blackburn, J. C. Johnson, N. R. Neale, *Chem. Mater.* **2015**, *27*, 6869.
[34] G. M. Carroll, R. Limpens, N. R. Neale, *Nano Lett.* **2018**, *18*, 3118.
[35] M. C. Schulze, N. R. Neale, *ACS Energy Lett.* **2021**, 1082.
[36] R. T. Pekarek, A. Affolter, L. L. Baranowski, J. Coyle, T. Hou, E. Sivonxay, B. A. Smith, R. D. McAuliffe, K. A. Persson, B. Key, C. Apblett, G. M. Veith, N. R. Neale, *J. Mater. Chem. A* **2020**, *8*, 7897.
[37] M. C. Schulze, G. M. Carroll, T. R. Martin, K. Sanchez-Rivera, F. Urias, N. R. Neale, *ACS Appl. Energy Mater.* **2021**, *4*, 1628.
[38] Y. Ha, T. R. Martin, S. Frisco, L. Rynearson, M. C. Schulze, S.-D. Han, S. E. Trask, B. L. Lucht, G. Teeter, N. R. Neale, *J. Electrochem. Soc.* **2022**, *169*, 070515.
[39] Y. Xu, K. Wood, J. Coyle, C. Engtrakul, G. Teeter, C. Stoldt, A. Burrell, A. Zakutayev, *J. Phys. Chem. C* **2019**, *123*, 13219.
[40] S. D. Han, K. N. Wood, C. Stetson, A. G. Norman, M. T. Brumbach, J. Coyle, Y. Xu, S. P. Harvey, G. Teeter, A. Zakutayev, A. K. Burrell, *ACS Appl. Mater. Interfaces* **2019**, *11*, 46993.
[41] J. Kim, O. B. Chae, B. L. Lucht, *J. Electrochem. Soc.* **2021**, *168*, 030521.
[42] M. Nie, D. P. Abraham, Y. Chen, A. Bose, B. L. Lucht, *J. Phys. Chem. C* **2013**, *117*, 13403.
[43] G. te Velde, F. M. Bickelhaupt, E. J. Baerends, C. Fonseca Guerra, S. J. A. van Gisbergen, J. G. Snijders, T. Ziegler, *J. Comput. Chem.* **2001**, *22*, 931.
[44] S. J. A. Van Gisbergen, J. G. Snijders, E. J. Baerends, *Comput. Phys. Commun.* **1999**, *118*, 119.